Irregular reflection of spark-generated shock pulses from a rigid surface: Mach-Zehnder interferometry measurements in air

Maria M. Karzova,[1,a)] Thomas Lechat,[2] Sébastien Ollivier,[3] Didier Dragna,[2] Petr V. Yuldashev,[1] Vera A. Khokhlova,[1] and Philippe Blanc-Benon[4]
[1]*Faculty of Physics, M. V. Lomonosov Moscow State University, Moscow 119991, Russia*
[2]*Université de Lyon, Ecole Centrale de Lyon, Laboratoire de Mécanique des Fluides et d'Acoustique, Unité Mixte de Recherche, Centre National de la Recherche Scientifique 5509, Ecully, F-69134, France*
[3]*Université de Lyon, Université Lyon 1, Laboratoire de Mécanique des Fluides et d'Acoustique, Unité Mixte de Recherche, Centre National de la Recherche Scientifique 5509, Ecully, F-69134, France*
[4]*Université de Lyon, Ecole Centrale de Lyon, Centre National de la Recherche Scientifique, Laboratoire de Mécanique des Fluides et d'Acoustique, Unité Mixte de Recherche 5509, F-69134, Ecully Cedex, France*

(Received 6 August 2018; revised 26 November 2018; accepted 3 December 2018; published online 3 January 2019)

The irregular reflection of weak acoustic shock waves, known as the von Neumann reflection, has been observed experimentally and numerically for spherically diverging waves generated by an electric spark source. Two optical measurement methods are used: a Mach-Zehnder interferometer for measuring pressure waveforms and a Schlieren system for visualizing shock fronts. Pressure waveforms are reconstructed from the light phase difference measured by the interferometer using the inverse Abel transform. In numerical simulations, the axisymmetric Euler equations are solved using finite-difference time-domain methods and the spark source is modeled as an instantaneous energy injection with a Gaussian shape. Waveforms and reflection patterns obtained from the simulations are in good agreement with those measured by the interferometer and the Schlieren methods. The Mach stem formation is observed close to the surface for incident pressures within the range of 800 to 4000 Pa. Similarly, as for strong shocks generated by blasts, it is found that for spherical weak shocks the Mach stem length increases with distance following a parabolic law. This study confirms the occurrence of irregular reflections at acoustic pressure levels and demonstrates the benefits of the Mach-Zehnder interferometer method when microphone measurements cannot be applied. https://doi.org/10.1121/1.5084266

[JDM] Pages: 26–35

I. INTRODUCTION

Irregular reflection is a classical phenomenon of shock wave physics first observed by Ernst Mach in 1875.[1] In Mach's reports, reflection of shock waves is categorized in two types: the two-shock configuration (regular reflection) and the three-shock configuration (Mach reflection). In the second case, the reflection pattern consists of three shocks: the incident and reflected shocks, which intersect above the surface, and the Mach stem, which connects the point of intersection to the surface. In 1943, these experimental observations were theoretically studied by von Neumann, who formulated two- and three-shock theories.[2]

Nowadays, a whole field of research is devoted to the study of irregular reflection of shock waves. The main feature of irregular reflection is the number of shocks in the reflection pattern, which is not equal to two. Basically, irregular reflection can be broadly divided into two types: Mach reflection and von Neumann reflection.[3] The shock strength can be characterized by the acoustic Mach number M_a, defined as the ratio of the maximum particle velocity of the acoustic wave to the speed of the ambient sound in the propagation medium. The Mach reflection effect is typical for strong shocks ($M_a > 0.47$) and has broad classification of possible reflection configurations.[3,4] The von Neumann reflection concerns weak acoustic shocks and occurs in the framework of the von Neumann paradox, whereas the three-shock theory either has no physically acceptable solutions or no solution at all.[3,5] The von Neumann reflection differs from the Mach reflection by the absence of slope discontinuity between the reflected shock and the Mach stem.[6] In the following, the "Mach stem" refers to the single shock that forms between the surface and the point where the incident shock and the reflected shock start to separate. Note that irregular reflections may exist for all shock pressure ranges and can be observed in gases, liquids, and even in solids.[7,8]

In this paper, we focus on the reflection of weak acoustic shock waves in the framework of the von Neumann paradox. In Ref. 6 the different reflection types of weak plane step-shock, saw-tooth wave, and *N*-wave have been studied in detail using numerical simulations based on the 2D Khokhlov-Zabolotskaya (KZ) equation.[9] Three possible types of nonlinear reflection were reported for weak acoustic shocks: nonlinear regular reflection, characterized by the presence of two shocks with different angles of incidence

[a)]Also at: Université de Lyon, Ecole Centrale de Lyon, Centre National de la Recherche Scientifique, Laboratoire de Mécanique des Fluides et d'Acoustique, Unité Mixte de Recherche 5509, Ecully, F-69134, France. Electronic mail: masha@acs366.phys.msu.ru

and of reflection, the von Neumann reflection, and the weak von Neumann reflection with no reflected shock at all. The type of reflection depends on the shock amplitude, the grazing angle θ of the plane incident wave, and the nonlinearity coefficient β of the propagation medium. Mathematically, this categorization is determined according to the critical parameter a introduced first in Ref. 10 as $a = \sin\theta/\sqrt{2\beta M_a}$. The transition from regular to irregular reflection types is reported to occur when the value of the critical parameter decreases to $a = \sqrt{2}$ for the step-shock and to about 0.8 for the plane N-wave.[6] These different reflection types have been experimentally observed in water for plane ultrasound sawtooth waves.[7] The same categorization of reflection types has also been found for shear shock waves in soft elastic solids.[8]

Except those generated in shock tubes, shock waves are generally not plane and have a more complicated morphology, often being closer to cylindrical or spherical waves. Examples would be focused ultrasound shock waves which are widely used in ultrasound therapy, sonic booms produced by aircraft, shock waves produced by supersonic projectiles, or blasts. For the last case, the shock wave has a spherical morphology and diverges spherically. However, to our knowledge, the irregular reflection of spherical weak acoustic shock waves has not been studied to the same extent as plane waves and strong shocks. The formation of the Mach stem for spherically diverging shock waves produced by a spark source was first observed numerically in Ref. 11. In our previous works, the reflection of spherical N-waves generated by sparks over flat rigid surfaces was studied numerically and experimentally using the Schlieren technique.[12,13] In this paper, previous experimental and numerical observations are improved and extended to longer propagation distances. In addition, waveforms in irregular reflection patterns are measured for the first time in air at pressure levels up to 10 kPa.

Since microphones disturb the pressure field and do not measure shocks accurately, optical methods must be used to observe reflection patterns and wavefront geometry. In aeroacoustics, optical methods are commonly used to visualize the structure of shock waves.[14] The basic principle of these methods is that acoustic waves induce variations in air density and consequently variations in the optical refractive index. As a result, the light beam deviates from its initial trajectory and acquires an additional optical phase difference when passing an acoustic wave.

In previous studies on shock wave reflections, optical methods were mainly used only for visualizing reflection patterns to determine the type of reflection.[15–18] Irregular reflection patterns and Mach stem formation can even be observed in one hundred-years-old photographs of pressure waves propagating in small room models.[19] However, in most cases, optical methods only provide a visualization of the location of shocks and do not provide a quantitative measure of pressure waveforms. It is recalled that the response of microphones does not allow for the detection of very rapid pressure variations during the passage of shocks. Also note that using microphones in a field with shocks will distort it and create additional reflections. Recently, it has been shown that in a homogeneous atmosphere it is possible to accurately reconstruct pressure signals from an electric spark source using optical techniques, in particular from Schlieren images or from interferometer measurements.[20,21] In addition, the temporal resolution of the interferometric method is 0.4 μs, which is 6 times higher than the resolution of a 1/8-in. condenser microphone (2.5 μs). This ability to reconstruct the pressure signature of acoustic shock waves using optical methods allows the study of waveforms at points of reflection, where usual microphone-based techniques cannot be applied.

The goal of this paper is to demonstrate that the interferometric method is capable of measuring waveforms in regular and irregular reflection patterns. The method is applied to a laboratory experiment where short shock pulses of about 35 μs duration are generated by an electric spark source. Validation of the interferometric method is performed by comparison with the results of numerical simulations based on the axisymmetric Euler equations and with reflection patterns obtained using the Schlieren technique. According to the categorization given in Ref. 6, three nonlinear reflection types shown in Fig. 1(a) are observed. These types are the regular reflection with unequal incident and reflected angles, the von Neumann reflection, and the weak von Neuman reflection. The interest here is focused on the von Neumann reflection type in which the Mach stem formation occurs. In this paper, we also pay attention to the evolution of the Mach stem length in the reflection process.

The content of the paper is organized as described as follows. Two experimental configurations based on the interferometry and Schlieren techniques are described first (Secs. II A and II B, correspondingly). Then, the numerical model is

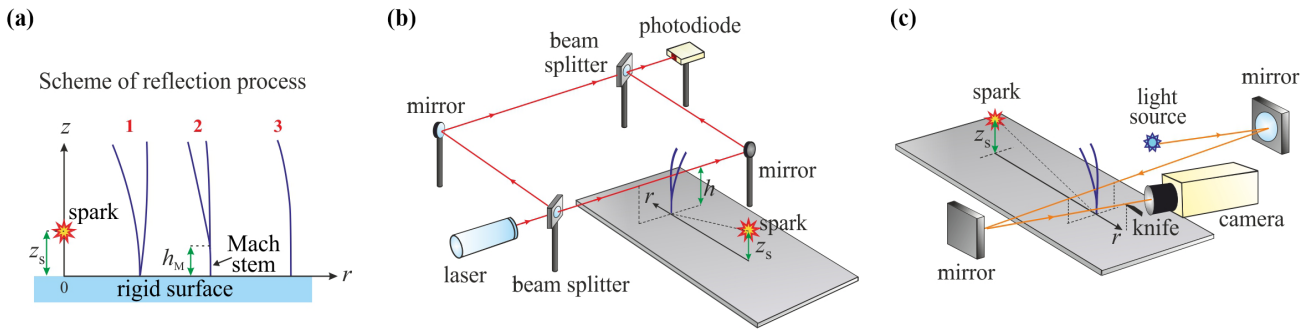

FIG. 1. (Color online) (a) Scheme illustrating the transition of nonlinear reflection types for weak acoustic shocks—1: regular reflection, 2: von Neumann reflection (irregular reflection), 3: weak von Neumann reflection (irregular reflection). (b), (c) Diagrams of experimental arrangements for measurements of reflection patterns in air: Mach-Zehnder interferometry method (b) and Schlieren technique (c).

presented (Sec. II C). In the results section, reconstructed waveforms from interferometric measurements (Sec. III A) and reflection patterns (Sec. III B) are analyzed and compared with simulated ones. Finally, the evolution of the Mach stem over the propagation distance is shown up to 70 cm from the spark source (Sec. III C). The results are summarized in Sec. IV.

II. MATERIALS AND METHODS

A. Mach-Zehnder interferometry method

A Mach-Zehnder optical interferometer is used to measure the pressure signature of shock waves. The method has been presented in detail in Ref. 21, here we only describe the experimental setup and summarize the optical signal processing performed for reconstructing the pressure waveforms.

The experimental setup includes acoustical and optical parts [Fig. 1(b)]. The sound source is an electrical spark positioned at a height of $z_s = 21$ mm above a plane rigid surface made of PVC. Considering the ratio of air and PVC impedances, the transmission is negligible and the surface is considered as perfectly reflecting. The spark source is made of two tungsten electrodes separated by a gap of 20 mm and supplied by an electrical voltage of 15–20 kV. The spark generates spherically divergent pressure waves that are similar to *N*-waves or blast waves.

The optical part is the Mach-Zehnder interferometer. As shown in Fig. 1(b), the main components are: a laser source (He-Ne laser, wavelength $\lambda = 632.8$ nm, nominal power 10 mW); two beam splitters (one separates the laser beam into two beams, and the second one collimates the two beams back into one); two mirrors; and a photodiode sensitive to the light intensity that results from the interference of the two beams (NT53–372, Edmund Optics, surface 3.2 mm^2, bandwidth 16 MHz).

The principle of the interferometer is to analyze the phase difference between the probing beam A, which crosses the acoustic wave, and the undisturbed reference beam B. The resulting light intensity measured by the photodiode is

$$I = I_A + I_B + 2\sqrt{I_A I_B}\cos\varphi, \tag{1}$$

where I_A and I_B are intensities of the probing and the reference beams, correspondingly, and φ is the optical phase difference between the two beams. The interferometer is first stabilized in the absence of the acoustic wave in such a way that the phase between the probing beam and the reference beam is $\varphi_0 = \pi/2$.

Neglecting light refraction and taking into account the radial symmetry of the wavefront, the optical phase difference φ_{ac} induced by the acoustic wave can be written as the direct Abel transform of the perturbation of the optical refractive index n (Ref. 21):

$$\varphi_{ac}(R,t) = \frac{4\pi}{\lambda}\int_R^\infty \frac{n(r_s,t)r_s \mathrm{d}r_s}{\sqrt{r_s^2 - R^2}}, \tag{2}$$

where R is the distance between the spark and the probing beam. The refractive index n is related to the perturbation of the air density ρ via the Gladstone–Dale constant G (Ref. 22): $n + n_0 = 1 + G(\rho + \rho_0)$, where ρ_0 is the ambient density and n_0 is the ambient refractive index. The experimental conditions are such that the acoustic pressure p is three orders of magnitude lower than the ambient atmospheric pressure. The density perturbation can therefore be considered as a linear function of the acoustic pressure p: $\rho = p/c_0^2$, where c_0 is the speed of sound. Thus, the refractive index is expressed as

$$n = Gp/c_0^2. \tag{3}$$

The measurement protocol is described below for the position of the probing beam above the rigid surface upon which acoustic waves reflect. Before each series of measurement, the system is calibrated. First, two output voltages u_A and u_B, which are respectively proportional to the intensities I_A and I_B, are measured separately in the absence of the acoustic wave. This is done by stopping the reference beam with a screen when measuring u_A and in the same way by stopping the probing beam when measuring u_B. Then, the bias voltage on the photodiode is shifted from zero to the value $(-u_A - u_B)$. Once the system is calibrated, the output voltage of the photodiode $u(t)$ is recorded when the probing beam is crossed by the acoustic wave. The output voltage signal $u(t)$ is induced by the interference of the reference and probing beams. It is expressed using the optical phase difference $\varphi = \varphi_0 + \varphi_{ac}$ as follows:

$$u(t) = 2\sqrt{u_A u_B}\sin\{\varphi_{ac}(t)\}. \tag{4}$$

By combining Eqs. (1)–(4) and applying the inverse Abel transform to Eq. (2), one obtains the following relation between the acoustic pressure $p(t)$ and the output voltages u_A, u_B, and u:

$$p(t) = -\frac{c_0^2\lambda}{2\pi^2 G}\int_R^\infty \frac{\mathrm{d}}{\mathrm{d}r_s}\left(\arcsin\frac{u\left(t_s - \frac{R - r_s}{c_0}\right)}{2\sqrt{u_A u_B}}\right)\frac{\mathrm{d}r_s}{\sqrt{r_s^2 - R^2}}, \tag{5}$$

where t_s is a constant time shift corresponding to the position of the front shock in the signal $u(t)$.

In experiments, 140 waveforms are recorded at each point in order to allow for statistical analysis of data. Because of small variations in the parameters of the generated waveforms (arrival time, peak positive pressure, and peak negative pressure) and because these parameters are not linearly related, it is counterintuitive to compute an average waveform from the 140 records. A better solution is therefore to statistically analyze waveform parameters (arrival time, peak of positive pressure, and negative peak) and to choose, among the 140 waveforms, the one whose parameters values are the closest to the average values computed over all waveforms. The selected waveform is hereinafter referred to as the "average" waveform. Technically, the average waveform is such that the sum of the relative error for the three previously mentioned parameters is the smallest. Since the method gives access to the waveform $p(t)$ at a single altitude above the reflecting surface, this procedure is

repeated for a series of probing beam positions above the surface in order to determine the pressure field.

The horizontal distance r between the spark source and the probe laser beam is varied from 10 up to 37 cm. Thus, for a given spark position ($z_s = 21$ mm) the angle of incidence is in the range from 3.2° to 11.9° and the corresponding value of the acoustic Mach number is in the range from 5×10^{-3} to 2.1×10^{-2}.

Considering the experimental conditions (relative humidity: 49%, temperature: 292 K, atmospheric pressure p_0: 100737 Pa), the Gladstone-Dale constant at 632.8 nm is $G = 2.26 \times 10^{-4}$ m^3/kg, the speed of sound is $c_0 = 343$ m/s, the nonlinearity coefficient β is 1.2, and the ambient density ρ_0 is 1.22 kg/m^3.

B. Schlieren visualization

Optical visualization of the spatial distribution of the acoustic field is performed by a Z-type Schlieren system [Fig. 1(c)].[13,14] The acoustical part of the experimental setup is the same as in the case of interferometric measurements. The source is 21 mm above the surface and r is in the range from 10 to 33 cm. The optical part includes two off-axis parabolic mirrors (15°, 108 mm diameter, 864 mm focal length), a continuous halogen white light source at the focus of the first mirror, and a knife edge at the focus of the second mirror in front of a high-speed Phantom V12 CMOS camera.

Schlieren images are recorded with a resolution of 650×500 pixels, a frame rate of 18 kHz and an exposure time of 1 μs. The brightness on images corresponds to the modulation of the light intensity and is proportional to the pressure gradient.[14] In order to improve the contrast of the Schlieren images, an averaged background image is calculated for each set of measurements and then is subtracted from each image containing reflection patterns.

The spatial accuracy of the Schlieren measurement is limited by both the resolution of the image and the exposure time of the high-speed camera. The spatial resolution is 0.15 mm per pixel. The exposure time is 1 μs, which corresponds to the propagation distance of 0.34 mm for the acoustic wave. These two uncertainties lead to a spatial error of 0.51 mm.

C. Numerical model

In the present work, the axisymmetric Euler equations are solved using a high order finite-difference time-domain (FDTD) algorithm developed in the field of computational aeroacoustics. These equations can be written in cylindrical coordinates (r, z) as

$$\begin{cases} \dfrac{\partial \tilde{\rho}}{\partial t} + \dfrac{\partial(\tilde{\rho} v_r)}{\partial r} + \dfrac{\partial(\tilde{\rho} v_z)}{\partial z} + \dfrac{\tilde{\rho} v_r}{r} = 0, \\ \dfrac{\partial(\tilde{\rho} v_r)}{\partial t} + \dfrac{\partial\left(\tilde{\rho} v_r^2 + \tilde{p}\right)}{\partial r} + \dfrac{\partial(\tilde{\rho} v_r v_z)}{\partial z} + \dfrac{\tilde{\rho} v_r^2}{r} = 0, \\ \dfrac{\partial(\tilde{\rho} v_z)}{\partial t} + \dfrac{\partial(\tilde{\rho} v_r v_z)}{\partial r} + \dfrac{\partial\left(\tilde{\rho} v_z^2 + \tilde{p}\right)}{\partial z} + \dfrac{\tilde{\rho} v_r v_z}{r} = 0, \\ \dfrac{\partial(\tilde{\rho} E)}{\partial t} + \dfrac{\partial(v_r\{\tilde{\rho} E + \tilde{p}\})}{\partial r} + \dfrac{\partial(v_z\{\tilde{\rho} E + \tilde{p}\})}{\partial z} + \dfrac{v_r\{\tilde{\rho} E + \tilde{p}\})}{r} = 0, \end{cases} \tag{6}$$

where $\tilde{p}$ is the total pressure, $\tilde{\rho}$ is the total density, and v_r and v_z are velocity components in the r and z directions, respectively [see Fig. 1(a)]. The total energy E is defined for a perfect gas as

$$\tilde{\rho} E = \frac{\tilde{p}}{\gamma - 1} + \tilde{\rho} \frac{v^2}{2}, \tag{7}$$

where $\gamma = 1.4$ is the specific heat ratio for diatomic air and $v = \sqrt{v_r^2 + v_z^2}$.

The time integration of Eqs. (6) is performed by an optimized second-order low-storage Runge-Kutta algorithm.[23] Spatial derivatives are evaluated by fourth order 11-point stencil finite-difference schemes. At the interior points, the centered schemes given in Ref. 23 are used. At the points near the boundaries of the computational domain, non-centered schemes[24] are used except at the $r = 0$ boundary, where the previously mentioned centered schemes are applied to enforce the axisymmetric condition. Both spatial and temporal methods are optimized in the Fourier space to minimize numerical dispersion and dissipation of the acoustic signal during long-range propagation. In addition, at each time step, a selective filter with an 11-point stencil is applied to suppress grid-to-grid oscillations.[24,25] The shock capturing methodology proposed in Ref. 25 and improved for the acoustic case in Ref. 26 is employed. It consists of a second order filter with a magnitude significant only around the shock and negligible everywhere else. The aim is to suppress signal components of excessively high frequencies that are generated by nonlinear effects. The strength of this filter and the selective filter are both set to 0.1. The boundary condition given at the flat surface, $z = 0$, is zero normal velocity. Finally, the radiation boundary conditions derived from asymptotic solutions of the linearized Euler equations in Ref. 27 are used to reduce reflections of the acoustic waves at the outer boundaries.

Simulations are carried out for a mesh of 1500×1500 points with spatial steps of $\Delta z = 0.1$ mm and $\Delta r = 0.05$ mm. The temporal step Δt is fixed at 0.45×10^{-7} s corresponding to a Courant-Friedrichs-Lewy number (CFL) around 0.3. A moving window is used to reduce computational costs.

The spark source is modeled as an instantaneous energy release with a Gaussian shape centered at the location ($r = 0$, $z_s = 21$ mm) in an atmosphere at rest where temperature, pressure, and density are elsewhere constant. The initial conditions for the numerical simulations are then given by

$$\begin{cases} \tilde{p}(r,z,t=0) = p_s \exp\left\{-\ln(2)\dfrac{r^2+(z-z_s)^2}{w^2}\right\} + p_0, \\ \vec{v}(r,z,t=0) = 0, \\ \tilde{\rho}(r,z,t=0) = \rho_0, \\ E(r,z,t=0) = \dfrac{\tilde{p}(r,z)}{\rho_0(\gamma-1)}. \end{cases} \tag{8}$$

The amplitude p_s and the half-width w of the Gaussian source have been first adjusted to fit the interferometric data measured in free field at different distances from the spark source, yielding $p_s = 0.75$ MPa and $w = 2.5$ mm. However, a better agreement between experimental and numerical results in the presence of the rigid surface has been obtained with a lower amplitude of the model source than what was derived by fitting the data in free field. Therefore, the numerical source amplitude is reduced to $p_s = 0.46$ MPa. The atmospheric pressure p_0 and the ambient density ρ_0 are set from the experimental data (Sec. II A). As in experiments, the source is 21 mm above the surface, but a larger distance range is considered as r is in the range from 0 to 70 cm.

III. RESULTS

In this section, experimental and numerical methods are applied to study the acoustic field resulting from the reflection of spark-generated waves from a plane rigid surface in air. Waveforms reconstructed from interferometric data are analyzed in detail and compared with those obtained by numerical simulations. Reflection patterns measured at different distances from the spark by the two optical methods are compared with those obtained in simulations. The evolution of the Mach stem with the propagation distance is studied up to 37 cm for the experiments and up to 70 cm for the numerical simulations.

A. Pressure waveforms: Irregular reflection

The pressure waveforms obtained at different heights h above the rigid surface at the distance $r = 13$ cm are shown in Fig. 2. Solid lines correspond to the waveforms reconstructed from interferometric measurements as described in Sec. II A. Recall that these waveforms are so-called "average" waveforms obtained from a series of 140 recordings for each measurement position. The dashed lines are simulation results, which correspond to virtual microphone outputs. Note that the temporal resolution of the Mach-Zehnder interferometric method (0.4 μs) is much smaller than that of a microphone or a weak shock pressure sensor. Another great advantage of the Mach-Zehnder interferometric method is that it does not disturb the investigation area unlike a membrane sensor. The size of the Mach stem that will be discussed below is in the order of the diameter of a microphone. Thus, only such optical method is capable of accurately capturing the details of pressure waveforms close to reflective boundary.

As seen in Fig. 2, at a height of 2 mm above the surface, the waveform shape is between the one of a blast wave and

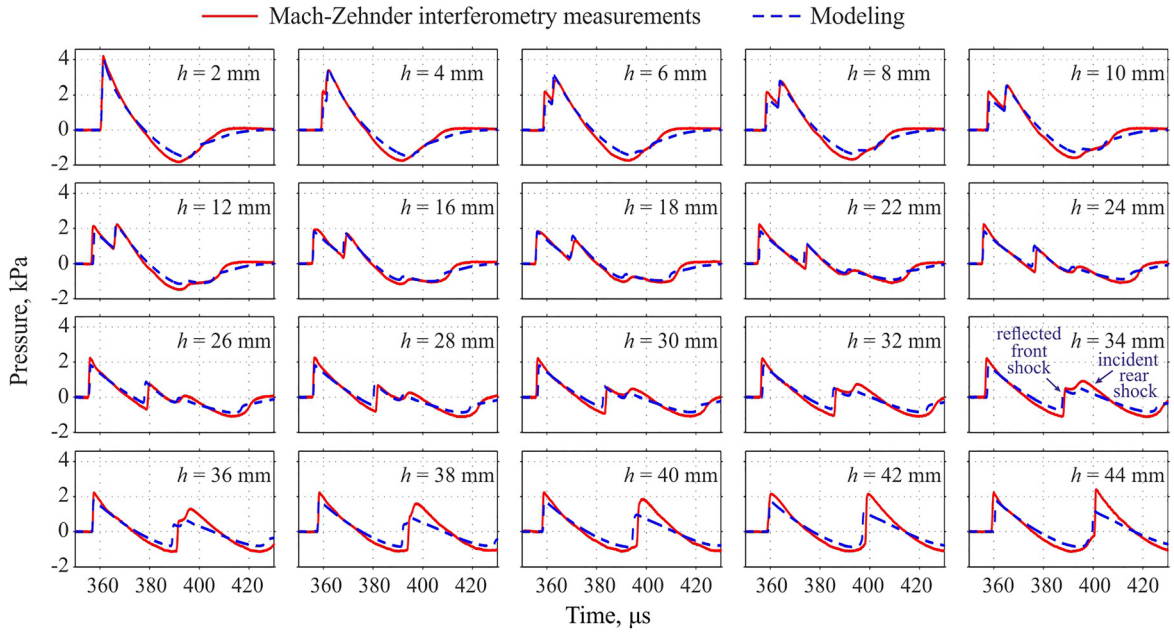

FIG. 2. (Color online) Pressure waveforms of spark-generated waves measured by the Mach-Zehnder interferometer (solid curves) and obtained from numerical simulations (dashed curves) at different heights h above the rigid surface at the distance $r = 13$ cm along the surface.

an N-wave. The positive phase begins with a steep shock front (named "front" or "leading" shock), followed by a gradual pressure decrease to zero after the peak pressure. Next there is a negative phase and finally the pressure returns back to equilibrium with a less steep pressure rise than that of the front shock. At 4 mm above the surface, the separation of the direct and reflected shocks starts to be observed at the front shock. Additional measurements with a finer analysis resolution in height confirm that only one shock is formed up to 3 mm height above the surface. Thus, the shock observed at $h = 2$ mm is the Mach stem. The reflection pattern for this case therefore corresponds to the irregular reflection type, and the height of the Mach stem is 3 ± 1 mm. The uncertainty is mostly related to the mechanical setup and signal analysis while the spatial resolution of the interferometer is in the order of only 0.2 mm. Note that the height of the Mach stem observed for this source and receiver position ($r = 13$ cm, $z_s = 21$ mm) is in strong agreement with the equation given in Ref. 13: $h_M = z_s(0.41/a)^2$, which was obtained from a series of simulations and experiments with the same spark source. With the parameter values of $a = 1.0194$ ($p_{max} = 2$ kPa, $M_a = 0.0143$, $\theta = 10.9°$) and $z_s = 0.021$ m this equation gives a Mach stem height of 3.4 mm.

For waves measured farther from the surface, from $h = 4$ to 32 mm, it can be noted that the reflected front shock is delayed until the delay corresponds to the duration of the wave, then it begins to merge with the pressure rise of the negative part (see frame at $h = 34$ mm). Similar to what is observed with strong shocks, the interaction of these two shocks well above the surface can be nonlinear and also lead to the formation of a single shock front (see Fig. 2, frame at $h = 42$ mm). Interestingly, at $h = 44$ mm, the waveform finally resembles two cycles of a saw-tooth wave.

The simulated waveforms (dashed lines in Fig. 2) are consistent with the measurements with good accuracy, especially for the front shock. The negative part is slightly less identical. Concerning the simulations, the Gaussian-envelope injection of energy used to simulate the spark source is a simplified model that accurately reproduces the positive impulse. However, it does not take into account neither the presence of electrodes nor hot gases generated during the discharge. Thus, the negative part of the initial pressure waveform is simulated less accurately. Above the surface, the initial difference in shape of the negative phase between the measured and simulated waveforms propagates and leads to a slight difference in the negative peak pressure (Fig. 2, see $h = 2$ mm and $h > 36$ mm).

Concerning the experimental method, one source of uncertainty is related to the value of distance R, which is used in the signal processing [Eq. (5)]. Actually, for measurement positions above the surface, the path lengths of the incident and reflected waves are different. However, this difference remains less than 10% for the configurations considered in the present study, so when applying Eq. (5) the value of R is chosen as the length of the direct path from the source to the measuring probe. However, as seen in Fig. 2, the difference between the simulated and measured pressure waveforms remains small, and does not exceed 10% for most part of the waveforms—which is comparable to the repeatability error of the spark source.

The simplified model of the spark source as a Gaussian energy injection combined with a nonlinear Euler equation propagation code yields time waveforms very close to the waveforms obtained from interferometric data and appropriate signal processing. Therefore, the methods are validated and applied to study the problem of irregular reflections.

B. Irregular reflection patterns

Interferometric and Schlieren techniques lead to different representations of the reflection patterns. The Schlieren technique provides photographs that show the location of the shock fronts in a plane, while the interferometric method provides information in the time domain (Figs. 3 and 4). Each Schlieren photograph captured by the high-speed camera is obtained with a single spark. In Schlieren images, the wave propagates from left to right and the wavefront is located on the right side of each image (Fig. 3). The contrast depends on the density gradient: the whitest areas correspond to the strongest pressure gradients. Thus, the different steepness of the front shock and the negative phase pressure rise leads to a different brightness. The reflection of the pressure rise of the negative phase is also visible, but as it is less steep, it is less bright. The reflection patterns obtained numerically correspond to the simulation of a single spark. The Schlieren pictures obtained numerically (Fig. 3, bottom) represent the gradient of the density of air, but in both r and z directions, while in the experiment, the gradient is only in the r direction.

The Schlieren images in Fig. 3 show the reflection patterns captured at different distances r along the surface. They show the dynamic character of irregular reflection: the Mach stem formed by the interaction of the direct and reflected front shocks develops during its propagation along the surface. Unlike the front shock, the reflection of the negative phase is always regular because of its smaller amplitude and smoother pressure rise. As expected, Fig. 3 shows a distinctive feature of nonlinear reflection: the angle of incidence and the angle of reflection are not equal.[3]

The Schlieren technique immediately provides an image of reflection patterns. However, the images do not show the pressure field but rather the density gradient of the air in a direction determined by the orientation of the knife edge. The method described for the case of the free field in Ref. 20 to estimate the pressure from the image does not apply here due to the geometry of the wavefront. In addition, the resolution in the temporal and spatial domains is limited by the settings of the camera and the optics. Thus, it is interesting to reconstruct the reflection patterns from interferometric data.

In the same way that the reflection patterns are plotted from hydrophone measurements,[7] the reflection patterns can be plotted in the spatio-temporal domain from the waveforms obtained with the Mach-Zehnder interferometer. The time domain reflection pattern is obtained from the average waveforms measured at different heights above the surface by converting the pressure amplitude into color and tracing the resulting horizontal color bar at the corresponding height.

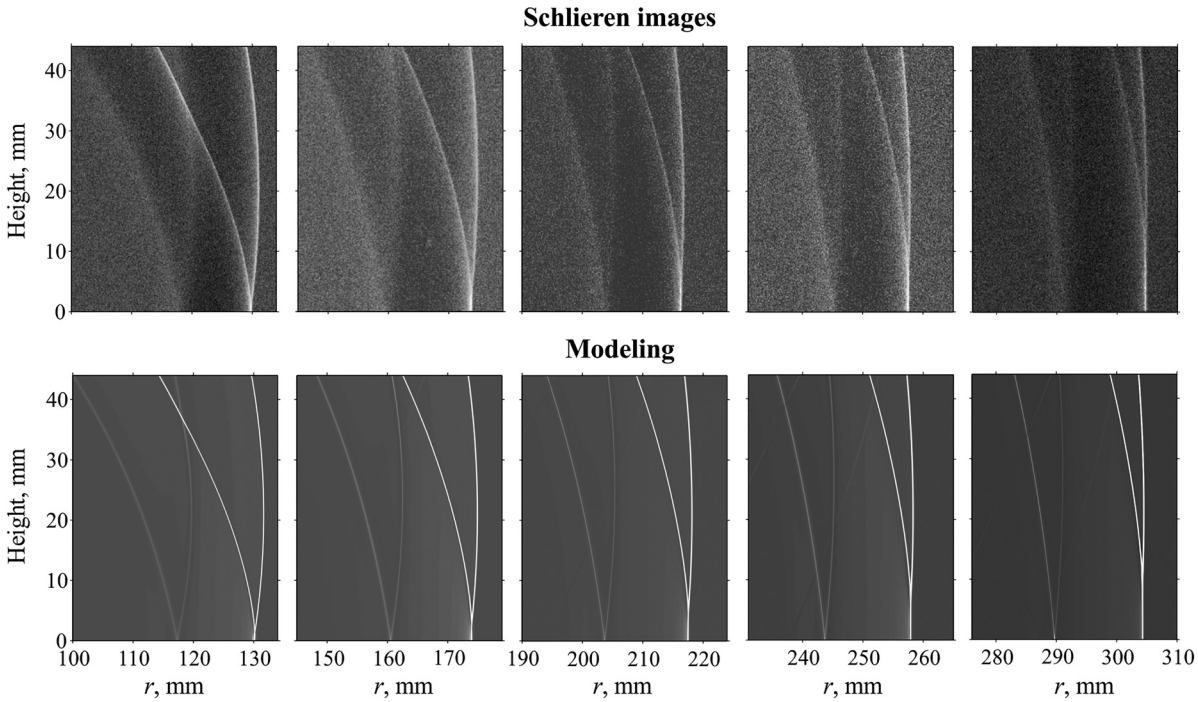

FIG. 3. Geometry of the reflection patterns visualized by Z-type Schlieren system (top row) and simulated numerically as a gradient of the density field (bottom row).

This means that each reflection pattern in the left column of Fig. 4 is obtained from a series of about three thousand sparks: 140 waveforms at each values of height h ranging from 2 up to 44 mm with a 2 mm step. Recalling that the spark source produces pulses with good repeatability[28] (variations in peak pressure and duration of about 10%), a reflection pattern obtained from average waveforms should be identical to that of a single spark. Unlike the reflection scheme obtained in the spatial domain with the Schlieren technique, the front shock appears on the left side of the image since it corresponds to the shortest propagation time (Fig. 4). Note that the color scale in the patterns obtained from the interferometric measurements represents the pressure, while the color scale of the Schlieren images represents the density gradient of the air in one direction and does not give information about pressure levels. The numerical interferometric spatio-temporal reflection patterns (Fig. 4, right column) are obtained from the pressure-time waveforms in Fig. 2 exactly as it was done for the experimental data.

For both optical methods, strong agreement is observed between the measured and simulated reflection patterns (Figs. 3 and 4). The front shock is reflected according to the irregular type of reflection and the Mach stem is formed near the surface. At the $r = 13$ cm position, the Mach stem is short, only about 3 mm as previously mentioned, but grows with the propagation distance and reaches the height of 13 mm at $r = 33$ cm (Fig. 4). The highest pressure levels are located just behind the Mach stems near the surface. At $r = 13$ cm, there is also an overpressure zone formed at the top of the figure, where the front shock of the reflected wave interacts with the rear shock of the incident wave (at approximately $t = 400\ \mu$s). As mentioned previously in Sec. III A, nonlinear interaction of shocks can also occur in this area in the same manner as the formation of the Mach stem on the reflecting surface.

C. Evolution of the Mach stem

In the reflection process, the length of the Mach stem changes with the propagation distance. In the context of blast wave studies, empirical models have been developed to predict the variation of the Mach stem length generated by the reflection of strong shock waves.[29] These models describe a parabolic[29] or a cubic[30] growth of the Mach stem height. Recent studies reporting experiments of weak shock reflection but at a larger scale than the present experiment showed a good agreement with a cubic law.[18] Although in our previous study with the same source a linear trajectory was reported,[13] that study was done for a small range of propagation distances r from 7 up to 13 cm. In the present study, the length of the Mach stem is analyzed from the three sets of data and at greater distances: with the Schlieren technique in the range from 10 up to 33 cm; with the interferometer in the range from 10 up to 37 cm, and with simulations up to 70 cm. The results are plotted in Fig. 5. Both optical methods and numerical simulations return approximately the same length of the Mach stem. The extension of the study to greater distances showed that the evolution of height of the Mach stem actually follows a parabolic law as expected from Ref. 29 rather than a linear law as done in Ref. 13. With the source parameters and positions considered in this study, a parabolic approximation $h_M = 0.104r^2 + 8.43 \times 10^{-3}r - 4.905 \times 10^{-4}$ is valid from $r = 0.1$ m up to 0.7 m, the maximum propagation distance where the simulations were carried out (inset of Fig. 5). Note that the distance of 70 cm corresponds to about 60 wavelengths.

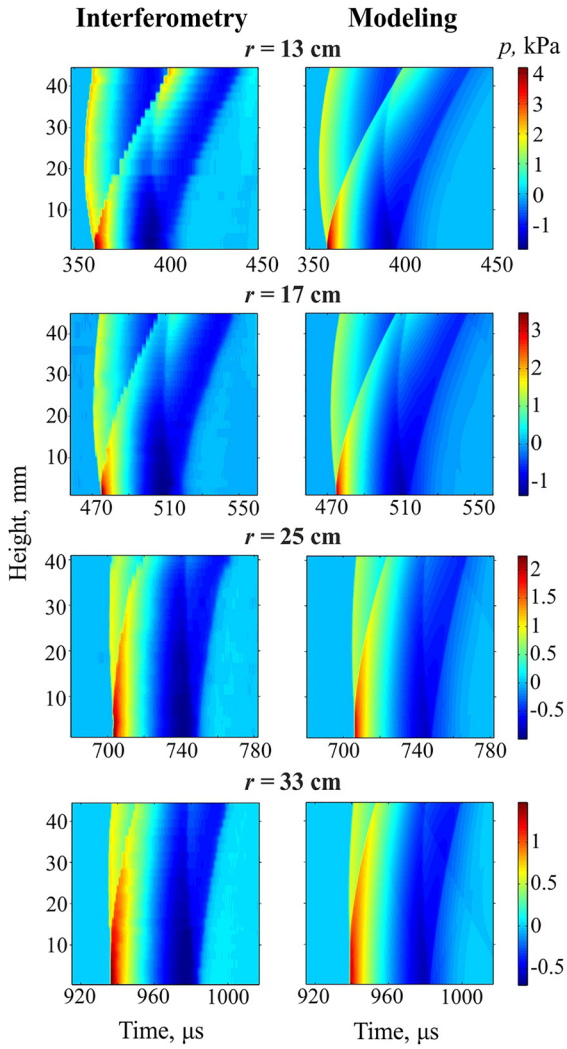

FIG. 4. (Color online) Reflection patterns measured by the Mach-Zehnder interferometer (left column) and obtained in numerical simulations based on axisymmetric Euler equation (right column). Reflection patterns are shown at different distances r along the surface.

The Mach stem starts to be formed at a distance $r = 10$ cm. At this distance, the peak positive pressure of the incident wave is 3 kPa. Estimating the value of the acoustic Mach number using its definition $M_a = p_{max}/(\gamma p_0)$ for the plane wave gives $M_a = 0.0214$. The value of the critical parameter is estimated from $a = \sin\theta/\sqrt{2\beta M_a}$, where the angle θ corresponds to the angle of incidence of the plane wave. The transition from the regular type of reflection to the irregular one occurs for the value of the critical parameter $a \approx 0.92$. This value agrees with our previous results[12,13] and also with corresponding transition for the plane N-wave obtained in numerical simulations based on the 2D KZ equation.[6]

Although the critical parameter a introduced in Refs. 6, 10 determines the reflection type only for plane waves, it includes two main physical effects involved in the Mach stem formation for waves of non-planar morphology. The first effect is the influence of the incident angle θ: for smaller angles the incident and reflected shocks are closer to each other and their nonlinear interaction that results in formation of only one shock can occur at smaller shock amplitudes

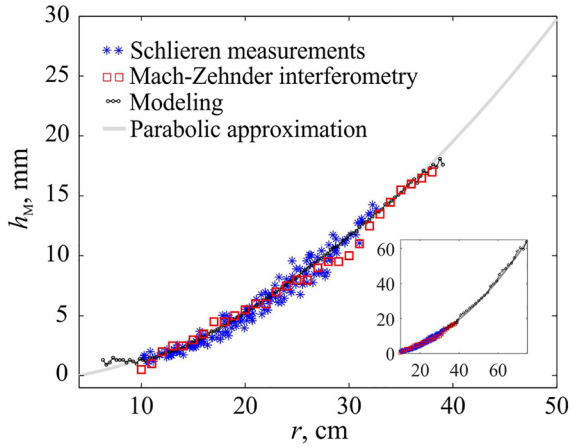

FIG. 5. (Color online) Evolution of the length of the Mach stem over the propagation distance r. Data are obtained from optical experiments using the Mach-Zehnder interferometer and Schlieren system as well as from numerical simulations. The parabolic approximation $0.104r^2 + 8.43 \times 10^{-3}r - 4.905 \times 10^{-4}$ given in meters was found to fit the trajectory.

than for larger incident angles. The second effect is the influence of the acoustic Mach number M_a which determines the strength of nonlinear effects. Since the Mach stem formation is a nonlinear phenomenon, it presents itself at smaller distances r for stronger shock waves. Both decrease of the incident angle and increase of the shock wave amplitude lead eventually to the Mach stem formation. Thus, the evolution of the Mach stem is strongly dependent on the evolution of θ and M_a.

For example, in the case of idealized plane step-shocks, both θ and M_a are constant along the propagation distance and hence the length of the Mach stem does not change. In the propagation of acoustic plane waves, like saw-tooth waves or N-waves, the shock amplitude decay occurs due to nonlinear absorption at the front shock while the incident angle θ remains constant. For this case the length of the Mach stem gradually decreases to zero since the value of the critical parameter a monotonically increases.

In the current paper, spherically diverging waves are considered. Such spherical morphology leads to continuous decrease of the incident angle θ. The evolution of the Mach stem is therefore determined by the competition between the influence of the incident angle θ and the decrease in amplitude due to both attenuation at the shock front and spherical divergence. To estimate the evolution of the Mach stem over long distances r one can use an approximation for grazing angles: $\sin\theta \approx \mathrm{tg}\ \theta = z_s/r$. Pressure decay for the current spark source has been studied previously in Refs. 20, 21, 28 and is described by the equation $p = p_{ref}(r/r_{ref})^{-\alpha}$, where p_{ref} is the pressure amplitude at the propagation distance r_{ref} and the coefficient $\alpha = 1.2$. In previous papers concerning spark sources,[31–33] the coefficient α is reported to be in the range of 1.2 to 1.4. Based on the knowledge of the pressure decay and angle approximation at long distances r the critical parameter a can be estimated as $a = \sin\theta/\sqrt{2\beta M_a} \approx r^{\alpha/2-1} z_s \sqrt{\gamma p_0/2\beta p_{ref} r_{ref}^{\alpha}}$, i.e., it is proportional to $r^{\alpha/2-1}$. For the given range of the coefficient α this dependence means that the critical parameter a decreases monotonically

with the propagation distance r. From this analysis one can conclude that the influence of the angle is more important than the decrease of the shock amplitude over the propagation distance. Thus, the reflection type remains irregular at long distances r up to a distance after which nonlinear effects are negligible.

In simulations and experiments at the laboratory scale, we indeed observe only the growth of the Mach stem until it is difficult to be distinguished. At long range, the weak von Neumann reflection is therefore obtained. We believe that the Mach stem evolves in the same way as described for strong shocks produced by explosions, for which its height only increases with the distance before the Mach stem eventually disappears as the grazing angle tends to zero.

IV. CONCLUSIONS

In this work, optical techniques were applied to measure the irregular reflection patterns of weak shock waves above a rigid plane surface. The Schlieren optical method, which is sensitive to the density gradient, provides the structure of the reflection pattern in the spatial domain. Mach-Zehnder interferometry with associated signal processing makes possible the reconstruction of pressure-time waveforms with spatial and temporal resolution that would not be achievable when using microphones. Having detailed knowledge of the characteristics of the source, it was possible to calibrate a source model based on an initial energy deposition. This source model, combined with a solver based on axisymmetric Euler equations, simulates the experiments with good precision. Both waveforms and reflection patterns obtained from optical measurements are in a good agreement with numerical simulations, providing a cross validation of both techniques to investigate nonlinear phenomena involving weak shocks. Thus, an instantaneous release of energy with a Gaussian shape is a suitable model for simulating spherical acoustic waves generated by a spark source, and a solver of the Euler equations is validated as a predictive tool to study nonlinear acoustic propagation and reflection phenomena. This approach can be generalized and applied to study problems with more complex geometries than a point source above a reflecting plane rigid surface.

Thanks to the temporal and spatial resolution of the Mach-Zehnder interferometer, it was possible to measure accurately the Mach stem height. The dynamics of irregular reflection were also observed over about 60 wavelengths, and the growth of the Mach stem was found to correspond to a parabolic law with the propagation distance along the surface—in the same manner as reported for stronger shocks. In the case of a spherical wave, it is expected that the height of the Mach stem, once formed, will increase until the incident wave and the reflected wave merge when the angle of incidence decreases to zero.

The present study was based on using a source that was well-known to the authors since it had been used in several previous experimental works. This choice allowed for cross-comparison of experimental and numerical data with already analyzed databases. However, the results are not limited to the current configuration but can be extended and generalized. From a metrological point of view, this study demonstrates that the spatial and temporal resolution of the Mach-Zehnder interferometric technique makes it possible to study phenomena at scales too small for microphones, in particular when shock waves are involved. From a physics point of view, these results show that irregular reflection occurs once the pressure waves are strong enough to generate shock waves and once the grazing angle is sufficiently low for a given peak pressure level. This phenomenon, well-known in the case of more intense shocks, can be observed for pressures on the order of 1 kPa, and must therefore be considered in nonlinear acoustics. Furthermore, given that it is impossible to observe this phenomenon using microphones, it is generally not considered in acoustics. Therefore, further experimental and numerical investigations with high temporal and spatial resolution techniques must be carried out to study nonlinear shock interactions at acoustic levels (peak pressure level between 1 and 10 kPa), and in cases with more complex geometries and surface characteristics, including rough and curved surfaces.

Connecting the results obtained in the present laboratory experiment with experiments at moderately larger scale[18] or with much strong blast waves is another perspective.

ACKNOWLEDGMENTS

Work supported by RSF-17-72-10277 and by the Labex CeLyA of Université de Lyon, operated by the French National Research Agency (ANR-10-LABX-0060/ ANR-11-IDEX-0007). The numerical study was conducted within the framework of LETMA (Laboratoire ETudes et Modélisation Acoustique), a Contractual Research Laboratory shared between CEA, CNRS, Ecole Centrale de Lyon, C-Innov, and Sorbonne Université. It was granted access to the HPC resources of IDRIS under the allocation 2017-82203 made by GENCI.

[1]P. Krehl and M. van der Geest, "The discovery of the Mach reflection effect and its demonstration in an auditorium," Shock Waves **1**(1), 3–15 (1991).
[2]J. Von Neumann, "Oblique reflection of shocks," in *John von Neumann Collected Work*, edited by A. H. Taub (MacMillan, New York, 1963), Vol. 6, pp. 238–299.
[3]G. Ben-Dor, *Shock Wave Reflection Phenomena*, 2nd ed. (Springer Verlag, New York, 2007), pp. 177–179.
[4]A. N. Semenov, M. K. Berezkina, and I. V. Krassovskaya, "Classification of pseudo-steady shock wave reflection types," Shock Waves **22**(4), 307–316 (2012).
[5]P. Colella and L. F. Henderson, "The von Neumann paradox for diffraction of a weak shock wave," J. Fluid. Mech. **213**, 71–94 (1990).
[6]S. Baskar, F. Coulouvrat, and R. Marchiano, "Nonlinear reflection of grazing acoustic shock waves: Unsteady transition from von Neumann to Mach to Snell-Descartes reflections," J. Fluid. Mech. **575**, 27–55 (2007).
[7]R. Marchiano, S. Baskar, F. Coulouvrat, and J.-L. Thomas, "Experimental evidence of deviation from mirror reflection for acoustical shock waves," Phys. Rev. E **76**, 056602 (2007).
[8]G. Pinton, F. Coulouvrat, J.-L. Gennisson, and M. Tanter, "Nonlinear reflection of shock shear waves in soft elastic media," J. Acoust. Soc. Am. **127**(2), 683–691 (2010).
[9]E. A. Zabolotskaya and R. V. Khokhlov, "Quasi-plane waves in the nonlinear acoustics of confined beams," Sov. Phys. Acoust. **15**, 35–40 (1969).
[10]M. Brio and J. K. Hunter, "Mach reflection for the two-dimensional Burgers equation," Physica D **60**, 194–207 (1992).

[11]V. W. Sparrow and P. Raspet, "A numerical method for general finite amplitude wave propagation in two dimensions and its application to spark pulses," J. Acoust. Soc. Am. **90**(5), 2683–2691 (1991).
[12]M. Karzova, V. Khokhlova, E. Salze, S. Ollivier, and P. Blanc-Benon, "Mach stem formation in reflection and focusing of weak shock acoustic pulses," J. Acoust. Soc. Am. **137**(6), EL436–EL442 (2015).
[13]C. Desjouy, S. Ollivier, O. Marsden, M. Karzova, and P. Blanc-Benon, "Irregular reflection of weak acoustic shock pulses on rigid boundaries: Schlieren experiments and direct numerical simulation based on a Navier-Stokes solver," Phys. Fluids **28**, 027102 (2016).
[14]G. S. Settles, *Schlieren and Shadowgraph Techniques: Visualizing Phenomena in Transparent Media* (Springer-Verlag, Heidelberg, 2001), pp. 27, 39–52, 338–340.
[15]B. Skews and J. Ashworth, "The physical nature of weak shock wave reflection," J. Fluid Mech. **542**, 105–114 (2005).
[16]T. Suzuki, T. Adachi, and S. Kobayashi, "Nonstationary shock reflection over nonstraight surfaces: An approach with a method of multiple steps," Shock Waves **7**, 55–62 (1997).
[17]Q. Wan, H. Jeon, R. Deiterding, and V. Eliasson, "Numerical and experimental investigation of oblique shock wave reflection off a water wedge," J. Fluid Mech. **826**, 732–758 (2017).
[18]K. M. Leete, K. L. Gee, and T. B. Nielsen, "Mach stem formation in outdoor measurements of acoustic shocks," J. Acoust. Soc. Am. **138**(6), EL522–EL527 (2015).
[19]S. Fischer, "A visual imprint of moving air: Methods, models, and media in architectural sound photography, ca. 1930," J. Soc. Arch. Hist. **76**(3), 326–348 (2017).
[20]M. Karzova, P. Yuldashev, V. Khokhlova, S. Ollivier, E. Salze, and P. Blanc-Benon, "Characterization of spark-generated *N*-waves in air using an optical schlieren method," J. Acoust. Soc. Am. **137**(6), 3244–3252 (2015).
[21]P. Yuldashev, M. Karzova, V. Khoklova, S. Ollivier, and P. Blanc-Benon, "Mach-Zehnder interferometry method for acoustic shock wave measurements in air and broadband calibration of microphones," J. Acoust. Soc. Am. **137**(6), 3314–3324 (2015).
[22]W. Merzkirch, *Flow Visualization* (Academic, New York, 1974), pp. 126–134.
[23]C. Bogey and C. Bailly, "A family of low dispersive and low dissipative explicit schemes for flow and noise computations," J. Comput. Phys. **194**(1), 194–214 (2004).
[24]J. Berland, C. Bogey, O. Marsden, and C. Bailly, "High-order, low dispersive and low dissipative explicit schemes for multiple-scale and boundary problems," J. Comput. Phys. **224**(2), 637–662 (2007).
[25]C. Bogey, N. de Cacqueray, and C. Bailly, "A shock-capturing methodology based on adaptative spatial filtering for high-order non-linear computations," J. Comput. Phys. **228**(5), 1447–1465 (2009).
[26]R. Sabatini, O. Marsden, C. Bailly, and C. Bogey, "A numerical study of nonlinear infrasound propagation in a windy atmosphere," J. Acoust. Soc. Am. **140**(1), 641–656 (2016).
[27]C. K. W. Tam and J. C. Webb, "Dispersion-relation-preserving finite difference schemes for computational acoustics," J. Comput. Phys. **107**(2), 262–281 (1993).
[28]P. Yuldashev, S. Ollivier, M. Averiyanov, O. Sapozhnikov, V. Khokhlova, and P. Blanc-Benon, "Nonlinear propagation of spark-generated *N*-waves in air: Modeling and measurements using acoustical and optical methods," J. Acoust. Soc. Am. **128**, 3321–3333 (2010).
[29]J. Boutillier, L. Ehrhardt, S. D. Mezzo, C. Deck, P. Magnan, P. Naz, and R. Willinger, "Evaluation of the existing triple point path models with new experimental data: Proposal of an original empirical formulation," Shock Waves **28**(2), 243–252 (2018).
[30]C. E. Needham, *Blast Waves* (Springer, New York, 2010), pp. 216–217.
[31]H. Honma, I. Glass, C. Wong, O. Holst-Jensen, and D. Xu, "Experimental and numerical studies of weak blast waves in air," Shock Waves **1**, 111–119 (1991).
[32]J. Reed, "Atmospheric attenuation of explosion waves," J. Acoust. Soc. Am. **61**, 39–47 (1977).
[33]L. Orenstein, "The rise time of N-waves produced by sparks," Technical Report No. ARL-TR-82-51, Applied Research Laboratories, University of Texas–Austin (1982).